Lawrence Berkeley National Laboratory
LBL Publications

Title
Characterizing Reactive Transport Behavior in a Three-Dimensional Discrete Fracture Network

Permalink
https://escholarship.org/uc/item/7084h8mt

Journal
Transport in Porous Media, 146(1-2)

ISSN
0169-3913

Authors
Sherman, Thomas
Sole-Mari, Guillem
Hyman, Jeffrey
et al.

Publication Date
2023

DOI
10.1007/s11242-021-01568-4

Peer reviewed

Characterizing Reactive Transport Behavior in a Three Dimensional Discrete Fracture Network

Thomas Sherman[1,2]**, Guillem Sole-Mari**[3,4]**, Jeffrey Hyman**[5]**, Matthew R. Sweeney**[5,6]**, Daniel Vassallo** [2,7]**, Diogo Bolster** [7]

[1]FTS International LLC, Dulles, VA

[2]Division of Environmental Research, CRCL Solutions LLC, South Bend, IN

[3]Geochemistry Department, Earth and Environmental Sciences Area, Lawrence Berkeley National Laboratory, Berkeley, CA

[4]Department of Civil and Environmental Engineering, Universitat Politècnica de Catalunya, Barcelona, Spain

[5]Computational Earth Science Group (EES-16), Earth and Environmental Sciences Division, Los Alamos National Laboratory, Los Alamos, NM 87545

[6]Center for Nonlinear Studies, Theoretical Division, Los Alamos National Laboratory, Los Alamos, NM, 87545

[7]Dept. of Civil and Environmental Engineering and Earth Sciences, University of Notre Dame, IN

Key Points:

- Discrete Fracture Network models are used to study reactive transport behavior.
- We consider the irreversible chemical reaction $A + B \rightarrow C$.
- Reactions primarily occur in the network backbone and reaction locations are sensitive to chemical properties.

Corresponding author: Thomas Sherman, `tjsherman24@gmail.com`

Abstract

While several studies have linked network and in-fracture scale properties to conservative transport behavior in subsurface fractured media, studies on reactive transport cases remain relatively underdeveloped. In this study, we explore the behavior of an irreversible kinetic reaction during the interaction of two solute plumes, one consisting of species A and the other species B. When the plumes converge, these species react kinetically to form a new species C via $A + B \xrightarrow{k} C$. This reactive system is studied using a three-dimensional discrete fracture network (DFN) model coupled with reactive Lagrangian particle tracking. We find that the interplay of network topology and chemical properties of the reactive solutes controls reactive transport processes. The network topology drives species A and B together and the chemical properties dictate whether and how quickly a reaction occurs. Results demonstrate that reactions are most likely to occur in high velocity fractures that make up the network backbone. The interplay between species' chemical properties and transport are characterized by a non-dimensional Damköhler (Da) number. We show that the spatial distribution of reactions is sensitive to Da, which subsequently influences late-time tailing behavior in outlet breakthrough time distributions. The results of this study provide initial insights into how an irreversible reaction occurs during transport in a fracture network, using a methodology that can be applied to study reactive transport in a wide range of fractured media environments and contexts.

1 Introduction

In low-permeability subsurface rocks, interconnected fracture networks control fluid flow and associated transport of dissolved chemical species (Bonnet et al., 2001). Heterogeneity in these systems occurs at multiple scales ranging from in-fracture scale properties (e.g., aperture roughness (Detwiler et al., 2000; Boutt et al., 2006; Cardenas et al., 2007; Kang et al., 2016; Bouquain et al., 2012)), to fracture scale properties (e.g., fracture lengths and orientations (de Dreuzy et al., 2001; Davy et al., 2006; Baghbanan & Jing, 2007; J. D. Hyman & Jiménez-Martínez, 2018)), to network structure, (e.g., density and connectivity (Bour & Davy, 1997; de Dreuzy et al., 2004; Maillot et al., 2016)). The interplay across multi-scale heterogeneities results in spatially variable flow fields within the network and, in turn, affects transport properties at the network scale (de Dreuzy et al., 2012; Frampton et al., 2019; Makedonska et al., 2016). Characterizing this heterogeneity and parameterizing it in high-fidelity modeling frameworks remains important for many engineering applications, including geothermal energy extraction (Pacala & Socolow, 2004), storage of spent nuclear fuel (Cvetkovic et al., 2004), CO_2 sequestration technologies (Barbier, 2002), groundwater risk assessment (Bolster et al., 2009), and groundwater remediation efforts (Steefel et al., 2005).

Discrete fracture network (DFN) models are a computational tool for simulating flow and transport in fractured media where geophysical features are directly represented rather than their upscaled equivalents (Berre et al., 2018). In a three-dimensional (3D) DFN, fractures are represented as 2D planar objects embedded in a 3D rock matrix that is considered impermeable and non-reactive. Governing equations for flow are numerically solved on a meshed representation of the DFN to solve for the velocity field within the network, which in turn allows for the simulation of transport. Explicitly representing the network structure requires more computational resources than conventional approaches, such as effective continuum models, but enables flow field structure and transport behavior to be directly linked to structural properties. To this end, a variety of studies have used DFN models to uncover the connections between geophysical, flow, and transport observations, thereby advancing our fundamental understanding of flow and transport in subsurface fractured media (Frampton & Cvetkovic, 2007; Frampton et al., 2019; de Dreuzy et al., 2012; J. D. Hyman et al., 2016; J. Hyman et al., 2019; J. D. Hyman,

Dentz, et al., 2019; Makedonska et al., 2016; Kang et al., 2017; Mourzenko et al., 2005; Sherman et al., 2019; Sherman, Hyman, et al., 2020).

To date, simulations in 3D fractured media have been largely devoted to the case of non-reactive (conservative) transport. However, understanding the interplay of geophysical structures and chemical reactions is critical for the successful advancement of our understanding of subsurface processes and applications, including each of those listed above. Given the DFN modeling success in linking geophysical features with conservative transport observations, a natural extension is to consider how network structure impacts reactive transport through fractured media. While a variety of reactive transport models have been developed to consider the interaction of two or more chemical species in heterogeneous porous media flows, e.g. equivalent continuum models (Knutson et al., 2007), effective kinetics models (Sanchez-Vila et al., 2010), fractional advection-dispersion equations (fADE) (Bolster et al., 2012), lamelar models (Anna et al., 2014; de Anna et al., 2014), particle tracking methods (Ding et al., 2013; Benson et al., 2017; Sund et al., 2017; Wright et al., 2017; Ding et al., 2017) and kernel density estimation approaches (Sole-Mari et al., 2017), they have yet be applied to flows in three-dimensional fracture network simulations.

In this study, we simulate irreversible kinetic reactions in a 3D DFN to provide a preliminary understanding of the connection between network structure and reactive transport. We simulate steady flow through a semi-generic fracture network topology using the DFNWORKS simulator (J. D. Hyman, Karra, et al., 2015). We consider an irreversible kinetic reaction with the form $A + B \rightarrow C$ and study reactive transport for different solute chemical properties by varying the system's Damköhler number Da, a non-dimensional number characterizing the ratio of diffusive to reactive time scales. Although this form is highly idealized, it serves as a foundational equation that can be expanded to understand more complex reactive processes (Gillespie, 1977). We consider a pulse injection of two plumes (one each species A and B) which have equal masses and placed into a steady-state flow field within the DFN. Species A and B are initially injected into separate regions of the DFN, but later converge via the flow structure. We observe the amount of species A, B, and C at the outlet plane as well as identify the specific timing and location of where reactions occur, and measure how behaviors vary based on the solute chemical properties as quantified via Da. It is important to note that reactive transport systems are much more sensitive to boundary and initial condition selections (Wood et al., 2000) and that different setups can behave quite differently (Valocchi et al., 2019), but that our chosen setup is an important end member that provides valuable initial insights.

In porous media, heterogeneity in the fluid velocity field results in reactive transport behavior that may significantly differ from that in a pure diffusive environment (Dentz et al., 2011; De Barros et al., 2012; Rolle & Le Borgne, 2019; Valocchi et al., 2019). For example, reactions can occur predominantly in hot-spot regions where velocity gradients are particularly strong (De Barros et al., 2012; Engdahl et al., 2017) or flow focusing occurs (Werth et al., 2006). Thus, in the context of fractured media we ask (i) how does spatial variability in the velocity field alter behavior relative to a pure diffusive system; (ii) how does the relative interplay of transport and reaction kinetics alter such behaviors and (iii) where do the majority of reactions occur? Our goal here is to present an initial modeling framework that can be used for reactive transport studies in subsurface fractured media and provide insights on how such behavior is influenced by network topological and chemical properties.

2 Numerical Simulations

2.1 Discrete Fracture Network Simulation

The three-dimensional fracture network is created using DFNWORKS (J. D. Hyman, Karra, et al., 2015). Network generation and meshing are performed using the feature rejection algorithm for meshing (FRAM) (J. D. Hyman et al., 2014), which produces a conforming Delaunay triangulation of the fracture network. The dual mesh of the triangulation, the Voronoi control volumes, are used by the massively parallel subsurface flow and transport code PFLOTRAN (Lichtner et al., 2015) to determine the steady state pressure solution within the network. An extension of the WALKABOUT particle tracking method (Makedonska et al., 2015; Painter et al., 2012) is used to determine pathlines through the DFN and simulate solute transport.
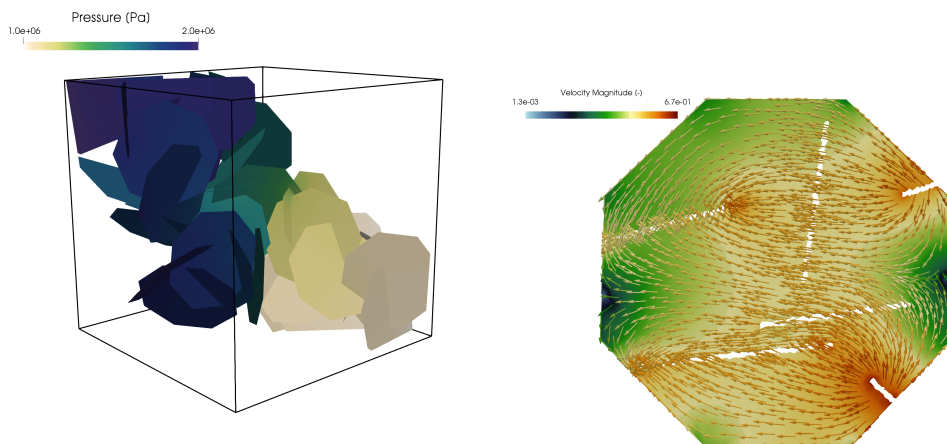
Figure 1. (Left) steady state pressure field in the entire DFN and (Right) the velocity vector field on a single fracture

We generate a generic three-dimensional fracture network composed of disc shaped fractures with radius of 1 m in a cubic domain of size 5 m × 5 m × 5 m. The fracture orientations and locations are uniformly random. Fracture apertures are uniform within each fracture and equal to $b = 10^{-4}$ m, which is a physically reasonable aperture value for a 1 meter fracture in crystalline rock (Svensk Kärnbränslehantering AB, 2010). Each fracture is meshed with a conforming Delaunay triangulation so the velocity field within each fracture can be fully resolved (J. D. Hyman et al., 2014). Flow in the fracture network is modeled using the Reynolds equation (Zimmerman & Bodvarsson, 1996), which provides volumetric flow rates and pressure values throughout the network (Fig. 1-left). The imposed pressure gradient is aligned with the x-axis, which is the primary direction of flow. These values are used to reconstruct a spatially variable velocity field $\mathbf{u}(\mathbf{x})$ at every mesh point in the network using the method of Painter et al. (2012) and Makedonska et al. (2015). Even though the fracture apertures are uniform within each fracture plane, the in-fracture velocity field can be highly non-uniform due to the complex network topology and boundary conditions imposed by the intersections with other fractures (Fig. 1-right).

Transport through the network is simulated using purely advective-particle tracking. We consider two solute plumes collectively consisting of $O(10^6)$ particles. Plume 1 consists solely of species A and plume 2 consists solely of species B. The two plumes are seeded on different inlet fractures and have approximately equal mass. We consider a pulse injection along the inlet plane where the unique initial positions of each particle

a is determined using flux-weighting (the concentration is proportional to the velocity at fracture-inlet intersections) (J. D. Hyman, Painter, et al., 2015; Kreft & Zuber, 1978). The trajectory $\mathbf{x}(t;\mathbf{a})$ of a particle starting at **a** at time $t = 0$ is given by the advection equation

$$\frac{d\mathbf{x}(t;\mathbf{a})}{dt} = \mathbf{v}(t;\mathbf{a}), \qquad \mathbf{x}(0;\mathbf{a}) = \mathbf{a}, \tag{1}$$

where the Lagrangian velocity $\mathbf{v}(t;\mathbf{x})$ is given in terms of the Eulerian velocity $\mathbf{u}(\mathbf{x})$. Local complete mixing is assumed to determine what fracture a particle exits onto when passing through intersections (Kang, Le Borgne, et al., 2015; Sherman et al., 2019).

2.2 Reactive Transport

The solute plumes consist of two species A and B who react to form a new species C via an irreversible kinetic reaction with the form A+B $\xrightarrow{k}$ C. Although highly idealized, we choose this simple reaction to elucidate the fundamental processes that influence reactive transport in fractured media, which could be overshadowed by more complex reaction chains.

Reactive transport is modeled from a Lagrangian perspective using the particle trajectories obtained in the steady-state flow field and chemical reactions are implemented in a probabilistic framework. The adopted numerical implementation is consistent with previous studies (Benson & Meerschaert, 2008; Paster et al., 2013, 2014; Bolster et al., 2016; Benson et al., 2019). In this method, the solute plume is conceptualized as an ensemble of particles, each with mass m_p. In order for two particles to react they must collocate due to transport. Recall that each particle trajectory is purely advective and streamlines cannot intersect. Therefore, we associate a local diffusion coefficient D with each particle that enables nearby particles to interact. This framework is acceptable in the regime of large Péclet numbers where advective effects dominate, which is reasonable in fractured media settings. Here, we define the Péclet number as

$$Pe = \bar{\mathbf{v}}l_c/D \tag{2}$$

where $\bar{\mathbf{v}}$ is the mean Lagrangian velocity 0.041m/s, $l_c = 1$m the average fracture radius, and we set $D = 10^{-3}$m^2/s, the latter of which is not chosen to reflect the properties of a specific chemical species but rather to explore a range of characteristic physical behaviors via non-dimensional analysis. In these simulations $Pe = 41$, an advection dominated regime.

In addition to the Péclet number, we also consider the Damköhler number Da defined using the ratio of diffusive and reactive timescales:

$$Da = \frac{kC_0 l_c^2}{D} \tag{3}$$

where C_0 is the initial concentration of solute. We study transport under a wide range of Da by changing the local reaction rate constant k and holding all other parameters constant. We consider Damköhler numbers of $10^2, 10^3, 10^4, 10^5$, and 10^6.

Benson and Meerschaert (2008) showed that the probability of reaction between two particles a distance s apart is

$$P_{\text{reaction}} = P_{\text{collocation}} P_{\text{react|coll}} = \frac{km_p}{8\pi D} \exp\left(-\frac{s^2}{8D\Delta t}\right), \tag{4}$$

where Δt is the numerical time step (1 s in this study). For each AB particle pair, a random number η is generated from a uniform distribution $U[0,1]$ and a reaction occurs when $\eta < P_{\text{reaction}}$. When a reaction occurs, the A and B particles react to form two C particles with mass m_p, thereby conserving mass in the system.

At each model step, the probability of reaction for all A and B particle pairs must be calculated, a potentially expensive numerical process, which is accelerated via a search tree algorithm (Paster et al., 2014). An AB particle pair may only react if they are located on the same fracture because impermeable rock separates fractures and so particles have effectively zero likelihood of reaction if separated by the rock matrix. Adding this constraint to the algorithm is both physically reasonable and more computationally efficient than searching all particle pairs. Note that during a given model time step, multiple A particles may have sufficient probability to react with the same B particle. In this case, we choose the AB pair with the highest $P_{\text{reaction}} - \eta$ value. We acknowledge that there may be additional constraints to consider, e.g. effects induced by fracture boundaries and intersections, and these are left for future development.

2.3 Measurements

The evolution of solute plume characteristics is tracked by measuring Lagrangian statistics at control planes set throughout the domain. Control planes are set perpendicular to the primary flow direction and are located at an equidistant spacing of $\Delta = 0.05$m, 1/100 the length of the domain in x. At each control plane (denoted x_j), we measure the first arrival time distribution, the transverse breakthrough distribution, and effective tortuosity for each particle defined using the equations below. These metrics enable characterization of plumes' spatio-temporal evolution and are used to quantify the influence of chemical reactions on transport behavior.

First Arrival Time Distribution: Denote the first arrival times of particles at the first crossing of control plane x_j as $\boldsymbol{\tau}_{x_j}$. We define the the first arrival time distribution at x_j as the cumulative distribution of $\boldsymbol{\tau}_{x_j}$,

$$\Psi(\mathbf{t})_{x_j} = \langle H(\mathbf{t} - \boldsymbol{\tau}_{x_j}) \rangle, \tag{5}$$

where H is the Heaviside function, and $\langle \rangle$ denotes the arithmetic average over all particles.

Transverse Breakthrough Position Distribution: Denote the transverse positions of particles at the first crossing of control plane x_j as $\mathbf{z}_{x_j}$. The transverse breakthrough position distribution (TBPD) $f(\mathbf{z}; x_j)$ at control plane x_j is defined as:

$$f(\mathbf{z}; x_j) = \langle \delta(\mathbf{z} - \mathbf{z}_{x_j}) \rangle \tag{6}$$

where $\delta(\mathbf{z})$ is the Dirac delta function. An analogous equation is used to calculate TBPD in y.

Effective Tortuosity: Let $\ell(x_j)$ be the total pathline distance from the network inlet of a particle upon its first crossing of a control plane at $x = x_j$. We define effective tortuosity between two control planes at x_i and x_j ($x_j < x_i$) as the ratio of pathline distance traveled by a particle between the control planes $\Delta\ell_{i,j} = |\ell(x_i) - \ell(x_j)|$ to the linear distance between those control planes $\Delta x_{i,j} = |x_i - x_j|$

$$\chi(x_{i,j}) = \frac{\Delta\ell_{i,j}}{\Delta x_{i,j}} . \tag{7}$$

Note particles are permitted to cross control plane x_j more than once before reaching x_i.

Effective tortuosity has been shown to be an important parameter for upscaling transport behaviors in recent studies (Sherman, Hyman, et al., 2020; Sherman, Janetti, et al., 2020). Here, effective tortuosity as we have defined it is a flow-dependent parameter that naturally aligns with our particle tracking approach; however it must be noted that there exist many other definitions for tortuosity in the literature (see for example (Ghanbarian et al., 2013)).

2.4 Graph-Based DFN Representation

In additional to the transport observables discussed in the previous section, we also consider the network structure. The topology (connectivity) of the network is characterized using a graph-based method where nodes in the graph correspond to fractures in the DFN and an edge between two nodes indicates that the corresponding fractures intersect (J. D. Hyman et al., 2017; Huseby et al., 1997; J. D. Hyman et al., 2018). The graph-representation of the DFN topology presented in Fig. 2 (left) shows that there are multiple paths from the inflow fractures (colored red and blue) and the outflow fractures, those connected to the green node. Additionally, there are a few dead-end regions of the DFN, which are represented as trees in the sub-graphs; a tree is an undirected graph where any two nodes are connected by exactly one path. Note that in three-dimensional DFNs there can be flow on dead-end fractures (J. D. Hyman, Jiménez-Martínez, et al., 2019) and thus these regions are not removed prior to simulating flow and transport. In the right subfigure, edge-sizes in the graph are proportional to the percentage of particles that pass between the corresponding intersection in the DFN with thicker lines indicating a larger number of particles. This graph representation is referred to as a flow topology graph (FTG) as it embeds the dynamics of the particle transport, which in this case represents the pathlines in the flow field, into the graph representation of the DFN (Aldrich et al., 2017).
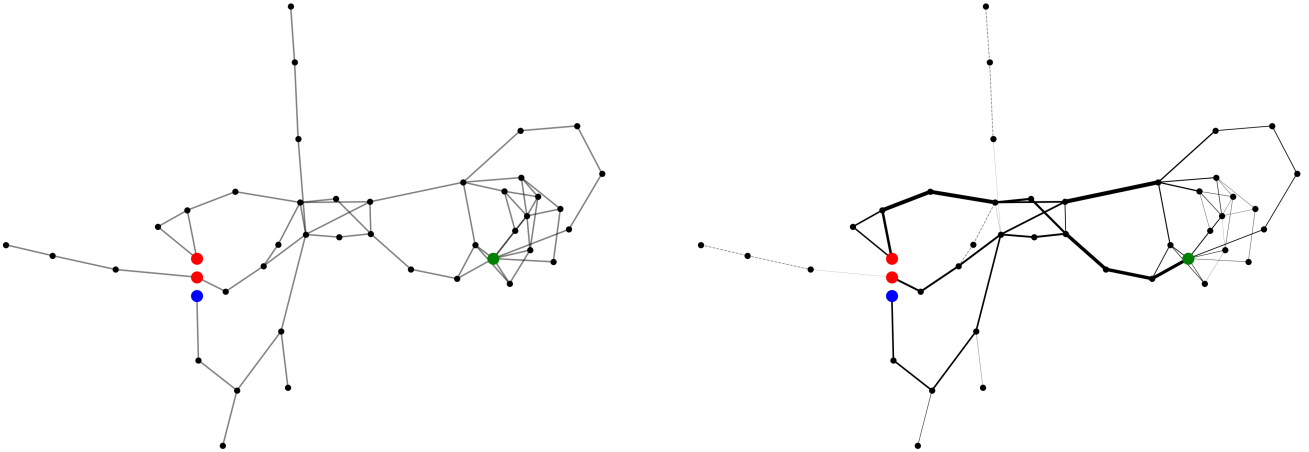
Figure 2. Topological (graph) representations of the DFN. (Left) Full network topology. Every node in the graph corresponds to a fracture in the DFN and an edge between two nodes indicates that the corresponding fractures intersect. The inflow fractures are colored blue and red and the outflow fracture is green. (Right) Flow topology graph with edge thickness proportional to the volumetric discharge.

3 Results

We begin the presentation of the results by considering a single Damköhler number (10^6) and then present the influence of Da on reactive transport behavior. Figure 3 displays the temporal evolution of the reactive solute plume for $Da = 10^6$: A particles are red, B particles are blue, and C particles are green. At early times, the particle A and B plumes have yet to converge and so no reactions occur; A and B plume dispersion is induced by local topology, which drives the heterogeneity in the velocity

field. By $t = 50s$ (bottom left subfigure), the fastest A and B particles reach the fractures where the flow field converges and react to produce C particles. After particles channelize through the fractures where the flow field converges, the network topology expands and branches, creating many possible pathways from the convergence fracture to network outlet. Both A and B particles traverse these pathways, enabling reactions to occur across the transverse spatial domain at later times.
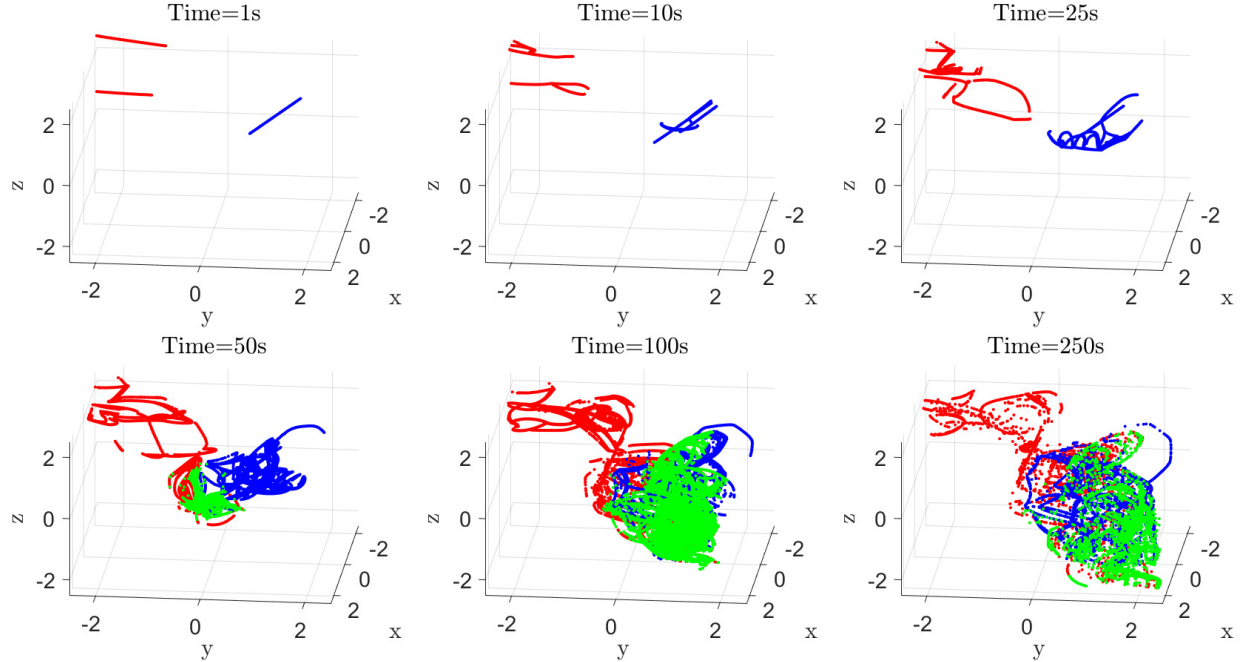
Figure 3. Snapshots of the solute plume at times 1, 10, 25, 50, 100, 250s for the $Da = 10^6$ case. A (red) and B (blue) particles react to form C (green) particles. At early times, no reactions have occurred because the A and B plumes have yet to converge. After sufficient time, the network topology channels particles to fractures where the flow field converges and reactions occur. In the above figure, particles are injected via a flux-weighted injection.

The influence of network topology on particle channelization and reactive transport becomes more clear via topological representations of the network. Figure 4 displays the possible paths for A (left), B (middle), and C (right) particles. Observe there exists a few primary pathways, depicted by thick lines, which control the majority of particle plume transport. Plumes A and B have separate primary pathways. However, when the A and B pathways converge, reactions become more probable, shown by green lines in the right subfigure. Reactions are limited to regions of the network where both A and B particles visit, e.g. reactions are not permitted in the far upper right of the network (Figure 4) because only A particles visit this network section.

The TBPD further demonstrates particle channelization. The top row of Figure 5 displays the TBPD for the y and z directions, i.e. we set control planes perpendicular to x and measure the transverse position of particle breakthrough at the first crossing of each control plane. Bright colors, corresponding to higher probability values, indicate regions of greater particle channelization. The bottom row displays the log probability of reaction for $x - y$ (left) and $x - z$ (right). Note that reactions only occur for $x > -0.5$ because the network topology does allow for the A and B solute plumes to
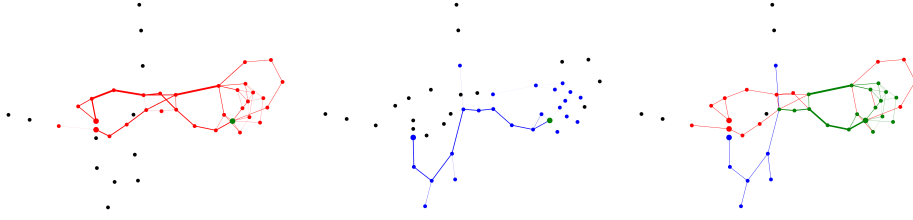
Figure 4. Topological representations of where particles pass through the DFN. Every node is a fracture and edges indicate particles pass between the two corresponding fractures. (left) A particles: Nodes and edges are colored red to show the paths of A particles. (middle) B particles: Nodes and edges are colored blue to show the paths of B particles. (right) Nodes and edges are colored green if both A and B particles pass through those fractures and intersections.

mix for x values closer to the inlet. Observe that the network regions with the highest reaction probability are also regions with high TBPD values, further demonstrating that reactions preferentially occur in primary pathways, where particles are channelized. Reactions become less likely near the network outlet. There is a reduced number of A and B particles that reach the outlet because many particles react earlier in the domain, thereby reducing the probability of reaction near the network outlet, i.e. particle reaction probability decreases as there are less particles available for reaction.

3.1 Influence of Damköhler Number

Table 1. The influence of Da on total number of reactions, the mean breakthrough time of C particles, the mean instantaneous particle velocity at the time of reaction, and mean topological distance for reactions, and mean network scale tortuosity for C particles.

Da	Total Reactions	$\bar{C}$ Breakthrough Time	$\bar{v}_{react}$	$\bar{d}_{topo}$	$\bar{\chi}_C$
[-]	[-]	[s]	[m/s]	[-]	[-]
10^2	326	303	0.05	5.6	1.23
10^3	2966	255	0.07	5.5	1.20
10^4	14688	213	.09	5.3	1.17
10^5	32416	192	.11	4.9	1.15
10^6	43834	190	.15	4.6	1.15

Reactive transport behavior is quantified for a range of Da spanning several orders of magnitude. Table 3.1 demonstrates the influence of Da on network scale transport metrics. Some general behavioral trends emerge: 1) as Da increases more reactions occur. 2) as Da increases, particles tend to react in high velocity channels; A and B particles with higher velocities are more likely to react, manifesting as faster C outlet breakthrough times for higher Da. 3) as Da increases, reactions tend to occur closer to the network inlet, as quantified with topological distance. The remainder of this section will explore these trends in more detail.

The total number of reactions that occur in the network increases with rising values of Da. In total there are 21 fractures where reactions occur in the studied network.
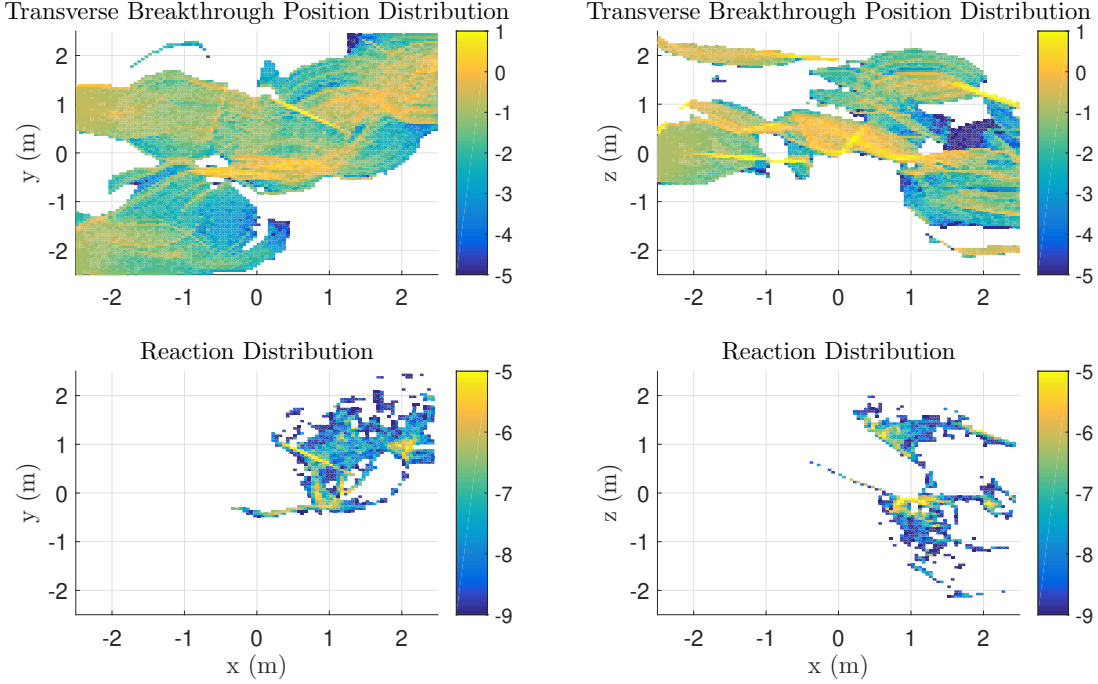
Figure 5. TBPD and Reaction location for $Da = 10^6$ and flux weighted boundary condition. Colors correspond to log probabilities.

But where those reactions occur depends on Da. Figure 6(left) shows the reactions per fracture number, where each fracture number is an identifier corresponding to a unique fracture. The fracture number is assigned from most to least reactions for the $Da = 10^6$ case, e.g., the most (least) reactions occur on fracture number 1 (21); note the fracture number mapping is defined uniquely based on the $Da = 10^6$ case and used for all other Da cases. The majority of reactions are confined to approximately 5 fractures, suggesting that a small portion of the network topology controls reactive transport processes. For example, in the $Da = 10^6$ case, more reactions occur on fracture 1 than the combined total number of reactions observed for fractures 7-21. These local reactive "hot spots" arise because the network topology and heterogeneity of the fluid velocity field leads to channelization of particles. Reactions only occur if the velocity field drives A and B particles together and so it is expected that fractures of high channelization are the most reactive spots in the network.

Additionally, the location of reactions is influenced by Da. As per our definition, the number of reactions as a function of fracture number must monotonically decrease for the $Da = 10^6$ case (as observed in Figure 6). However, for other Da cases, the number of reactions as a function of fracture number does not monotonically decrease, which demonstrates that the spatial distribution of reactions changes with Da.

The graph representation of the network topology enables us to calculate the minimum topological distance of each fracture, defined as the minimum number of edges connecting the graph inlet to a specific node/fracture. Figure 6(right) displays the histogram of reactions plotted as a function of topological distance. For the $Da = 10^6$ case, the number of reactions are maximized at a lower topological distance of 3, corresponding to the topological distance where the A and B particle paths first converge. For the other Da cases considered, the maximum number of reactions occur at a larger topological dis-
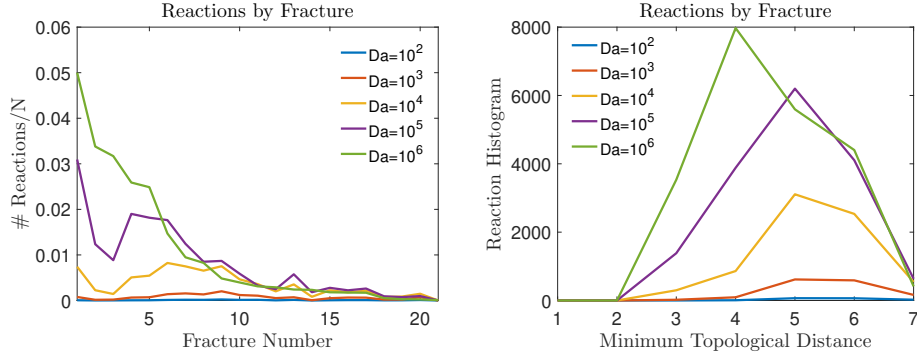
Figure 6. (Left) The number of reactions (normalized by the total number of particles N) at each fracture. Fracture number is ordered from most reactions to least in the $Da = 10^6$ case. Increasing the Da increases the total number of reactions that occur. Changing Da influences the location of reactions in the network. (Right) A histogram of reactions by minimum topological distance for different Da. Minimum distance for each reaction corresponds to the fracture where the reaction occurred. Da influences the location of reactions in the network.

tance of 5. This observation is copacetic with the previous observations that reactions occur further downstream with lower values of Da, because reactions kinetics are slower relative to transport time scales. In all Da cases, reactions are most likely near the fractures where the A and B plumes first converge. Hence, these reactions diminish the concentration of A and B particles at early topological distances, making less solute available for reactions at fractures later in the network. Such behavior manifests as a decrease in reactions for fractures with higher topological distances.
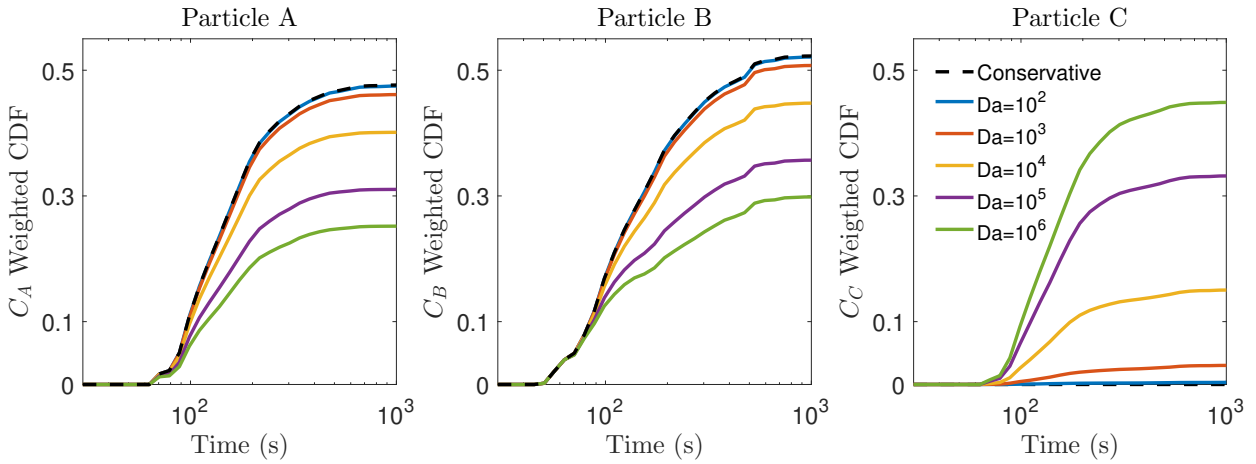
Figure 7. CDFs of particle outlet breakthrough times for A,B, and C species under a wide range of Da. CDFs weights are proportional to the total number of particles of each species. As Da increases, total particle C production increases.

Next, we investigate the influence of Da on outlet breakthrough time CDFs for A, B, and C particles over a wide range of Da (Figure 7). CDFs are normalized by the total number of particles, meaning after the last particle breakthrough, the summation of A, B, and C CDFs equals unity. As Da increases, the number of reactions increases and

subsequently the total number of C particles that exit the domain increases. When Da is small $O(100)$, reactions have negligible effect on solute breakthrough, illustrated by a nearly identical CDF with the conservative case. Da significantly influences C break-through curve behavior. There is inherently more particles in fast velocity channels and so when Da increases, A and B particles traversing these channels are the most likely to react; slow flow zones have lower particle concentrations and so slow particles are less likely to react. This creates a bias, where fast particles are more likely to react than slower ones. Various studies have demonstrated that fast channels persist at the network scale (Kang, Le Borgne, et al., 2015; Kang et al., 2016; J. Hyman et al., 2019; J. D. Hyman, 2020), meaning particles are likely to react in these channels and then persist at a high velocity until the network outlet; as Da increases, fast A and B particles preferentially react and slow ones do not. This bias manifests as a decrease in mean particle C plume breakthrough time with increasing Da; the mean (median) C plume arrival time is 189 (157), 192 (157), 213 (162), 255 (175), 303 (187) s for the $Da = 10^6, 10^5, 10^4, 10^3, 10^2$ cases. Consequently, the slowest particles in the network are less likely to react and so the A and B particle plumes have slower mean breakthrough times as Da increases.
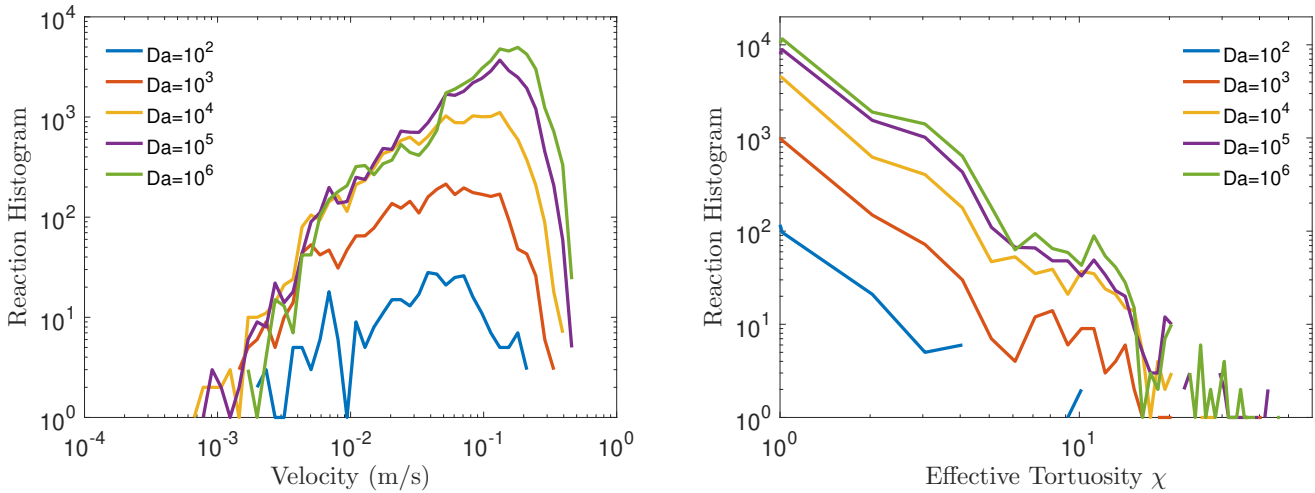
Figure 8. The left subfigure shows a histogram of reaction for different velocities for a range of Da. Reactions preferentially occur in high velocity regimes. The right figure displays reaction histograms for different effective tortuosities. Reactions are more likely in low tortuosity zones, which correspond to network primary pathways.

Particle channelization is closely related to high velocity regions of the network. High velocity regions directly translate to larger discharge rates (recall apertures are uniform), and subsequently more particles enter these high velocity regions. Hence, reactions can preferentially occur in these faster moving waters. Figure 8 (left) shows the instantaneous velocity of particles at the time of reaction via a histogram. The Lagrangian velocities at which reactions take place spans approximately 3 orders of magnitude, and the number of reactions in each velocity class spans several orders of magnitude. The most reactions occur at relatively fast velocities $O(10^{-1})$ m/s (recall, the mean velocity is 0.04m/s), further suggesting that high velocity fractures channelize particles and are locations of enhanced reactive behavior. As Da increases, the reaction distribution shifts to faster velocities; the peak reaction (90% CDF values) are 0.3 (.10), 0.5 (.14), .13 (.17), .13 (.22), and .18 (.26) m/s for $Da = 10^2, 10^3, 10^4, 10^5, 10^6$, respectively. This further demonstrates that the spatio-temporal reaction distribution is sensitive to Da.

Effective tortuosity quantifies the distance a particle travels in the transverse directions, meaning a particle's effective tortuosity tends to increase when its current fracture's orientation angle increases relative to the primary direction of flow or the flow field streamlines meander, such as in recirculation zones. Recall, particles traversing primary channels display lower tortuosity values on average than other fractures in the network, as these channels typically algin with the primary flow direction and can span the network scale (Sherman, Hyman, et al., 2020). Figure 8 (right) shows a histogram of reactions for different effective tortuosities. As the effective tortuosity increases, reactions become less likely for all Da. This suggests that reactions preferentially occur in the primary pathways of fracture networks, as those fractures are aligned with the primary pressure gradient and form the fastest velocity fractures, which is copacetic with the previous observations. The trend of increased reactions at fast velocities - low tortuosities provides further evidence that reactions preferentially occur in the primary channels of the network's backbone. These results demonstrate that Lagrangian tortuosity statistics are linked to reactions, which may be important for developing upscaled reactive transport models (more details to follow in discussion).

4 Discussion

The results of the simulations demonstrate that reactive transport is controlled by both the topology of the network and local chemistry within the fracture planes. Reactions can only occur if the solute A and B plumes are driven together, which depends on the network structure. Once the A and B solute plumes sufficiently mix, the spatio-temporal distribution of reactions is dictated by local diffusion and the chemical reaction rate. Such findings improve current characterization of reactive transport processes in subsurface fractured media and provide important implications for developing the next generation of upscaled reactive transport models.

4.1 Network Topology

The network topology plays an important role in reactive transport in two ways: 1) dissolved solute species can only react if the network topology enables the A and B solute plumes to collocate and 2) the heterogeneity of the fluid velocity field channelizes particles, thereby creating regions of enhanced mixing and reactions. Reactive transport behavior is therefore a function of network connectivity and particle channelization. While the second of these points has been investigated in numerous studies in heterogeneous porous media, the first point is unique to fracture networks.

In this study, the A and B solute plumes originate at separate inlet fractures. The two plumes can only interact if the network topology connects the inlet fractures to a common fracture, i.e. the possible A and B paths from network inlet to outlet must overlap for reactions between A and B species to occur. Therefore, the network connectivity is a principal control for the occurrence of reactions. The network considered here contains a fracture of convergence, where the network constricts to a single fracture that all particles must traverse. This fracture of convergence was demonstrated to be a region of enhanced reactions (Figure 4), as both A and B plumes are channelized here. If the network connectivity increased, we would expect reactions to occur earlier in the network, e.g. the first reactions would occur at a lower minimum topological distance.

Additionally, it has been well studied that large, high velocity fractures form primary pathways which serve as a network's backbone and control conservative transport behavior at the network scale (Kang, Dentz, et al., 2015; J. D. Hyman et al., 2017; Viswanathan et al., 2018; Kang et al., 2019; Sweeney & Hyman, 2020). However, study of the network backbone's role in reactive transport behavior has been limited. In this study, we observe that the primary pathways that comprise the network backbone are regions of high particle channelization; in these channels, reactive species are driven together and reac-

tions become increasingly likely. Intuitively, reaction probability increases when the concentration of A and B increases, which is exactly what happens in primary pathways. The channelization phenomena is visually apparent in Figure 5, where areas displaying a large number of reactions are highly correlated with areas of high TBPD values. Evidence for the correlation between channelization and reactions is further shown by reactions preferentially occurring in high velocity, low tortuosity regions of the network. Consequently, the spatial distribution of reactions is highly heterogeneous and focused where high particle channelization is prevalent. Hence, reactive transport processes are enhanced when the network topology both connects the A and B solute plumes, as well as concentrates the plumes at local in-fracture scales via flow channelization.

4.2 Particle Chemical Properties

While the network topology brings dissolved species together, reactions only occur if the chemical properties of those species are conducive for reactions. Diffusion is the mechanism by which nearby particles can collocate. In this study, we quantify diffusive and reactive timescales with Da, where the probability of reaction increases with increasing Da. Reaction probability goes to zero when $Da = 0$ (and $Pe \to \infty$), regardless of the network topological characteristics, because reactive transport behavior ultimately depends on the chemical properties of the solute species considered.

In this study, we observe that the spatial distribution of reactions is sensitive to Da. In the most reactive $Da = 10^6$ case, nearby particles have a relatively high probability to react and so a significant number of reactions occur when the A and B primary pathways first converge. This immediately diminishes the supply of available reactive species. As Da decreases, less reactions occur when the two plumes initially converge, leaving more reactive material at subsequent downstream fractures. This therefore shifts the locations of reactions to positions farther from the inlet (as shown by an increase in mean minimum topological distance for reactions). Evidence for this change in fracture location is also shown by a shift in the reaction-velocity distributions, where the mean velocity during the time of reactions increases with Da, suggesting reactions are occurring at different locations within the network.

The change in spatial reaction patterns with varying Da is important for larger scale reactive behavior. Faster particles react under increasing Da, meaning the A and B particles that do not react and reach the network outlet are slower on average than in the conservative case. This is clear in Figure 7, where mean C (A and B) breakthrough time decreases (increases) as Da increases. These results demonstrate that species' chemistry at the in-fracture scale propagates to the larger network scale and can influence the spatial-temporal distribution of reactions. Note, the results presented here consider a fixed Pe and future studies must address the influence of Pe on reactions before generalizing trends.

4.3 Implications for Upscaled Reactive Transport Models

Running reactive transport simulations with the DFN framework demands large computational resources. The benefit of such high-fidelity simulations is that reactive transport behavior can be described in great detail. However, ideally the transport behaviors observed in this and similar studies will be used to inform effective upscaled reactive transport models, which can be run with significantly reduced computational costs. Although we do not develop any upscaled models explicitly in this study, we provide some possible paths forward for developing the next generation of upscaled reactive transport models.

One key finding is that the majority of reactions are confined to a small percentage ($< 10\%$) of the fractures in the network and these key fractures help make up the network backbone. Previous studies have demonstrated that a graphical representation,

448 where each fracture is represented with an edge and corresponding mean velocity, may
449 be sufficient to predict the bulk conservative transport behavior (Karra et al., 2018; Valera
450 et al., 2018; Srinivasan et al., 2019). This graph theory upscaling method has not yet
451 considered reactive transport. However, given that the majority of reactions are located
452 in the network backbone where the graphical representation provides an accurate model,
453 there will be exciting opportunities to extend reactive transport to graphical represen-
454 tations in future work. The missing component of including reactive transport in graph-
455 ical representations is the probability that two particles react when traversing the same
456 network edge. We envision this can be accomplished with a method similar to the one
457 presented in this paper, where particles have a probability (based on separation distance)
458 of reacting if traversing a fracture at the same time.

459 Additionally, we observe that reactions preferentially occur in the high velocities
460 fractures that form the network's backbone; the corresponding particle trajectories travers-
461 ing the backbone typically display local low tortuosity values of $O(1)$. Recently, stud-
462 ies have shown continous time random walk models that consider the the Lagrangian velocity-
463 tortuosity correlation structure can accurately predict transport in fractured media (Kang
464 et al., 2019; Sherman, Hyman, et al., 2020) and porous media with adsoprtion-desoprtion
465 processes (Sherman, Janetti, et al., 2020). A natural extension of the correlated random
466 walk framework is to use this same velocity-tortuosity correlation structure to data mine
467 reaction probabilities, and upscale reactive transport in fractured media. Such an ap-
468 proach would leverage the fact that high velocity – low tortuosity particles are more likely
469 to react than slow velocity – high tortuosity particles. The exact details regarding this
470 implementation are saved for later work.

5   Remarks

472 This study provides a first investigation into how an irreversible kinetic reaction
473 influences the migration of a solute plume in a discrete fracture network framework. We
474 observed that the interplay of network topology and solute chemical properties are prin-
475 cipal controls of reactive transport behavior in fracture networks. Specifically, reactions
476 are most probable in high velocity pathways, where particles are channelized and there-
477 fore more likely to interact with other chemical species; then once species are brought
478 together by the topology, the local chemical properties dictate whether a reaction will
479 occur. The results and findings from this study, however, must not be generalized, as we
480 only considered one network structure and one type of initial condition. To character-
481 ize the influence of network structural properties on reactive transport behavior, future
482 studies must consider the range of network properties, e.g. fracture density, connectiv-
483 ity, permeability, etc. Likewise a variety of initial and boundary conditions should be ex-
484 plored. Additionally, we only consider an idealized chemical reaction. Fortunately this
485 idealized reaction takes a general form that can be easily adapted to consider reactions
486 between a wide variety of species observed in field-scale measurements. This work pro-
487 vides validation of a foundational methodology that can be extended to explore reactive
488 transport behavior in many future DFN studies.

498   https://github.com/lanl/dfnWorks LA-UR-20-26548

References

Aldrich, G., Hyman, J. D., Karra, S., Gable, C. W., Makedonska, N., Viswanathan, H., . . . Hamann, B. (2017). Analysis and visualization of discrete fracture networks using a flow topology graph. IEEE Transactions on Visualization and Computer Graphics, 23(8), 1896–1909. doi: 10.1109/tvcg.2016.2582174

Anna, P. d., Jimenez-Martinez, J., Tabuteau, H., Turuban, R., Le Borgne, T., Derrien, M., & Meheust, Y. (2014). Mixing and reaction kinetics in porous media: An experimental pore scale quantification. Environmental science & technology, 48(1), 508–516.

Baghbanan, A., & Jing, L. (2007). Hydraulic properties of fractured rock masses with correlated fracture length and aperture. International Journal of Rock Mechanics and Mining Sciences, 44(5), 704–719.

Barbier, E. (2002). Geothermal energy technology and current status: an overview. Renew. Sust. Energ. Rev., 6(1-2), 3–65.

Benson, D. A., Aquino, T., Bolster, D., Engdahl, N., Henri, C. V., & Fernandez-Garcia, D. (2017). A comparison of eulerian and lagrangian transport and non-linear reaction algorithms. Advances in Water Resources, 99, 15–37.

Benson, D. A., & Meerschaert, M. M. (2008). Simulation of chemical reaction via particle tracking: Diffusion-limited versus thermodynamic rate-limited regimes. Water Resources Research, 44(12).

Benson, D. A., Pankavich, S., & Bolster, D. (2019). On the separate treatment of mixing and spreading by the reactive-particle-tracking algorithm: An example of accurate upscaling of reactive poiseuille flow. Advances in Water Resources, 123, 40–53.

Berre, I., Doster, F., & Keilegavlen, E. (2018). Flow in fractured porous media: A review of conceptual models and discretization approaches. Transport Porous Med., 1–22.

Bolster, D., Barahona, M., Dentz, M., Fernandez-Garcia, D., Sanchez-Vila, X., Trinchero, P., . . . Tartakovsky, D. M. (2009). Probabilistic risk analysis of groundwater remediation strategies. Water Resources Research, 45(6), n/a–n/a. Retrieved from `http://dx.doi.org/10.1029/2008WR007551` (W06413) doi: 10.1029/2008WR007551

Bolster, D., de Anna, P., Benson, D. A., & Tartakovsky, A. M. (2012). Incomplete mixing and reactions with fractional dispersion. Advances in Water Resources, 37, 86–93.

Bolster, D., Paster, A., & Benson, D. A. (2016). A particle number conserving lagrangian method for mixing-driven reactive transport. Water Resources Research, 52(2), 1518–1527.

Bonnet, E., Bour, O., Odling, N. E., Davy, P., Main, I., Cowie, P., & Berkowitz, B. (2001). Scaling of fracture systems in geological media. Rev. Geophys., 39(3), 347–383.

Bouquain, J., Méheust, Y., Bolster, D., & Davy, P. (2012). The impact of inertial effects on solute dispersion in a channel with periodically varying aperture. Physics of Fluids, 24(8), 083602.

Bour, O., & Davy, P. (1997). Connectivity of random fault networks following a power law fault length distribution. Water Resources Research, 33(7), 1567–1583.

Boutt, D. F., Grasselli, G., Fredrich, J. T., Cook, B. K., & Williams, J. R. (2006). Trapping zones: The effect of fracture roughness on the directional anisotropy of fluid flow and colloid transport in a single fracture. Geophysical Research Letters, 33(21).

Cardenas, M. B., Slottke, D. T., Ketcham, R. A., & Sharp, J. M. (2007). Navier-

Stokes flow and transport simulations using real fractures shows heavy tailing due to eddies. Geophys. Research Lett., 34(14).

Cvetkovic, V., Painter, S., Outters, N., & Selroos, J. (2004). Stochastic simulation of radionuclide migration in discretely fractured rock near the äspö hard rock laboratory. Water Resources Research, 40(2).

Davy, P., Bour, O., De Dreuzy, J.-R., & Darcel, C. (2006). Flow in multiscale fractal fracture networks. Geological Society, London, Special Publications, 261(1), 31–45.

de Anna, P., Dentz, M., Tartakovsky, A., & Le Borgne, T. (2014). The filamentary structure of mixing fronts and its control on reaction kinetics in porous media flows. Geophysical Research Letters, 41(13), 4586–4593.

De Barros, F. P., Dentz, M., Koch, J., & Nowak, W. (2012). Flow topology and scalar mixing in spatially heterogeneous flow fields. Geophysical Research Letters, 39(8).

de Dreuzy, J., Darcel, C., Davy, P., & Bour, O. (2004). Influence of spatial correlation of fracture centers on the permeability of two-dimensional fracture networks following a power law length distribution. Water Resources Research, 40(1).

de Dreuzy, J., Davy, P., & Bour, O. (2001). Hydraulic properties of two-dimensional random fracture networks following a power law length distribution 2. permeability of networks based on lognormal distribution of apertures. Water Resources Research, 37(8), 2079–2095.

de Dreuzy, J., Méheust, Y., & Pichot, G. (2012). Influence of fracture scale heterogeneity on the flow properties of three-dimensional discrete fracture networks. J. Geophys. Research-Sol. Ea., 117(B11).

Dentz, M., Le Borgne, T., Englert, A., & Bijeljic, B. (2011). Mixing, spreading and reaction in heterogeneous media: A brief review. Journal of contaminant hydrology, 120, 1–17.

Detwiler, R. L., Rajaram, H., & Glass, R. J. (2000). Solute transport in variable-aperture fractures: An investigation of the relative importance of taylor dispersion and macrodispersion. Water Resources Research, 36(7), 1611–1625.

Ding, D., Benson, D. A., Fernàndez-Garcia, D., Henri, C. V., Hyndman, D. W., Phanikumar, M. S., & Bolster, D. (2017). Elimination of the reaction rate "scale effect": Application of the lagrangian reactive particle-tracking method to simulate mixing-limited, field-scale biodegradation at the schoolcraft (mi, usa) site. Water Resources Research, 53(12), 10411–10432.

Ding, D., Benson, D. A., Paster, A., & Bolster, D. (2013). Modeling bimolecular reactions and transport in porous media via particle tracking. Advances in water resources, 53, 56–65.

Engdahl, N. B., Benson, D. A., & Bolster, D. (2017). Lagrangian simulation of mixing and reactions in complex geochemical systems. Water Resources Research, 53(4), 3513–3522.

Frampton, A., & Cvetkovic, V. (2007). Upscaling particle transport in discrete fracture networks: 1. nonreactive tracers. Water Resources Research, 43(10).

Frampton, A., Hyman, J., & Zou, L. (2019). Advective transport in discrete fracture networks with connected and disconnected textures representing internal aperture variability. Water Resources Research. Retrieved from https://agupubs.onlinelibrary.wiley.com/doi/abs/10.1029/2018WR024322 doi: 10.1029/2018WR024322

Ghanbarian, B., Hunt, A. G., Ewing, R. P., & Sahimi, M. (2013). Tortuosity in porous media: a critical review. Soil science society of America journal, 77(5), 1461–1477.

Gillespie, D. T. (1977). Exact stochastic simulation of coupled chemical reactions. The journal of physical chemistry, 81(25), 2340–2361.

Huseby, O., Thovert, J., & Adler, P. (1997). Geometry and topology of fracture sys-

tems. J. Phys A-Math Gen, 30(5), 1415.

Hyman, J., Dentz, M., Hagberg, A., & Kang, P. K. (2019). Linking structural and transport properties in three-dimensional fracture networks. Journal of Geophysical Research: Solid Earth, 124(2), 1185–1204.

Hyman, J. D. (2020). Flow channeling in fracture networks: Characterizing the effect of density on preferential flow path formation. Water Resour. Res..

Hyman, J. D., Aldrich, G., Viswanathan, H., Makedonska, N., & Karra, S. (2016). Fracture size and transmissivity correlations: Implications for transport simulations in sparse three-dimensional discrete fracture networks following a truncated power law distribution of fracture size. Water Rescour. Research, 52(8), 6472–6489. Retrieved from `http://dx.doi.org/10.1002/2016WR018806` doi: 10.1002/2016WR018806

Hyman, J. D., Dentz, M., Hagberg, A., & Kang, P. (2019). Emergence of stable laws for first passage times in three-dimensional random fracture networks. Phys. Rev. Lett., 123(24), 248501.

Hyman, J. D., Gable, C. W., Painter, S. L., & Makedonska, N. (2014). Conforming Delaunay triangulation of stochastically generated three dimensional discrete fracture networks: A feature rejection algorithm for meshing strategy. SIAM J. Sci. Comput., 36(4), A1871–A1894.

Hyman, J. D., Hagberg, A., Osthus, D., Srinivasan, S., Viswanathan, H., & Srinivasan, G. (2018). Identifying backbones in three-dimensional discrete fracture networks: A bipartite graph-based approach. Multiscale Modeling & Simulation, 16(4), 1948–1968.

Hyman, J. D., Hagberg, A., Srinivasan, G., Mohd-Yusof, J., & Viswanathan, H. (2017). Predictions of first passage times in sparse discrete fracture networks using graph-based reductions. Phys. Rev. E, 96(1), 013304. doi: 10.1103/PhysRevE.96.013304

Hyman, J. D., & Jiménez-Martínez, J. (2018). Dispersion and mixing in three-dimensional discrete fracture networks: Nonlinear interplay between structural and hydraulic heterogeneity. Water Rescour. Research, 54(5), 3243-3258.

Hyman, J. D., Jiménez-Martínez, J., Gable, C. W., Stauffer, P. H., & Pawar, R. J. (2019). Characterizing the impact of fractured caprock heterogeneity on supercritical co2 injection. Transport in Porous Media, 1–21.

Hyman, J. D., Karra, S., Makedonska, N., Gable, C. W., Painter, S. L., & Viswanathan, H. S. (2015). dfnWorks: A discrete fracture network framework for modeling subsurface flow and transport. Comput. Geosci., 84, 10–19.

Hyman, J. D., Painter, S. L., Viswanathan, H., Makedonska, N., & Karra, S. (2015). Influence of injection mode on transport properties in kilometer-scale three-dimensional discrete fracture networks. Water Resources Research, 51(9), 7289–7308.

Kang, P. K., Brown, S., & Juanes, R. (2016). Emergence of anomalous transport in stressed rough fractures. Earth Planet. Sc. Lett., 454, 46–54.

Kang, P. K., Dentz, M., Le Borgne, T., & Juanes, R. (2015). Anomalous transport on regular fracture networks: Impact of conductivity heterogeneity and mixing at fracture intersections. Physical Review E, 92(2), 022148.

Kang, P. K., Dentz, M., Le Borgne, T., Lee, S., & Juanes, R. (2017). Anomalous transport in disordered fracture networks: spatial Markov model for dispersion with variable injection modes. Adv. Water Resources, 106, 80–94.

Kang, P. K., Le Borgne, T., Dentz, M., Bour, O., & Juanes, R. (2015). Impact of velocity correlation and distribution on transport in fractured media: Field evidence and theoretical model. Water Resources Research, 51(2), 940–959.

Kang, P. K., Lei, Q., Dentz, M., & Juanes, R. (2019). Stress-induced anomalous transport in natural fracture networks. Water Resources Research.

Karra, S., O'Malley, D., Hyman, J., Viswanathan, H., & Srinivasan, G. (2018). Modeling flow and transport in fracture networks using graphs. Phys. Rev. E,

97(3), 033304.

Knutson, C., Valocchi, A., & Werth, C. (2007). Comparison of continuum and pore-scale models of nutrient biodegradation under transverse mixing conditions. Advances in Water Resources, 30(6-7), 1421–1431.

Kreft, A., & Zuber, A. (1978). On the physical meaning of the dispersion equation and its solutions for different initial and boundary conditions. Chemical Engineering Science, 33(11), 1471–1480.

Lichtner, P., Hammond, G., Lu, C., Karra, S., Bisht, G., Andre, B., . . . Kumar, J. (2015). PFLOTRAN user manual: A massively parallel reactive flow and transport model for describing surface and subsurface processes (Tech. Rep.). (Report No.: LA-UR-15-20403) Los Alamos National Laboratory.

Maillot, J., Davy, P., Le Goc, R., Darcel, C., & De Dreuzy, J.-R. (2016). Connectivity, permeability, and channeling in randomly distributed and kinematically defined discrete fracture network models. Water Resources Research, 52(11), 8526–8545.

Makedonska, N., Hyman, J. D., Karra, S., Painter, S. L., Gable, C. W. W., & Viswanathan, H. S. (2016). Evaluating the effect of internal aperture variability on transport in kilometer scale discrete fracture networks. Adv. Water Resources, 94, 486–497.

Makedonska, N., Painter, S. L., Bui, Q. M., Gable, C. W., & Karra, S. (2015). Particle tracking approach for transport in three-dimensional discrete fracture networks. Computat. Geosci., 1–15.

Mourzenko, V., Thovert, J.-F., & Adler, P. (2005). Percolation of three-dimensional fracture networks with power-law size distribution. Phys. Rev. E, 72(3), 036103.

Pacala, S., & Socolow, R. (2004). Stabilization wedges: solving the climate problem for the next 50 years with current technologies. Science, 305(5686), 968–972.

Painter, S. L., Gable, C. W., & Kelkar, S. (2012). Pathline tracing on fully unstructured control-volume grids. Computat. Geosci., 16(4), 1125–1134.

Paster, A., Bolster, D., & Benson, D. (2013). Particle tracking and the diffusion-reaction equation. Water Resources Research, 49(1), 1–6.

Paster, A., Bolster, D., & Benson, D. A. (2014). Connecting the dots: Semi-analytical and random walk numerical solutions of the diffusion–reaction equation with stochastic initial conditions. Journal of Computational Physics, 263, 91–112.

Rolle, M., & Le Borgne, T. (2019). Mixing and reactive fronts in the subsurface. Reviews in Mineralogy and Geochemistry, 85(1), 111–142.

Sanchez-Vila, X., Fernàndez-Garcia, D., & Guadagnini, A. (2010). Interpretation of column experiments of transport of solutes undergoing an irreversible bimolecular reaction using a continuum approximation. Water Resources Research, 46(12).

Sherman, T., Hyman, J. D., Bolster, D., Makedonska, N., & Srinivasan, G. (2019). Characterizing the impact of particle behavior at fracture intersections in three-dimensional discrete fracture networks. Physical Review E, 99(1), 013110.

Sherman, T., Hyman, J. D., Dentz, M., & Bolster, D. (2020). Characterizing the influence of fracture density on network scale transport. Journal of Geophysical Research: Solid Earth.

Sherman, T., Janetti, E. B., Guédon, G. R., Porta, G., & Bolster, D. (2020). Upscaling transport of a sorbing solute in disordered non periodic porous domains. Advances in Water Resources, 103574.

Sole-Mari, G., Fernàndez-Garcia, D., Rodríguez-Escales, P., & Sanchez-Vila, X. (2017). A kde-based random walk method for modeling reactive transport with complex kinetics in porous media. Water resources research, 53(11), 9019–9039.

Srinivasan, S., Karra, S., Hyman, J., Viswanathan, H., & Srinivasan, G. (2019). Model reduction for fractured porous media: a machine learning approach for identifying main flow pathways. Computational Geosciences, 23(3), 617–629.

Steefel, C. I., DePaolo, D. J., & Lichtner, P. C. (2005). Reactive transport modeling: An essential tool and a new research approach for the earth sciences. Earth and Planetary Science Letters, 240(3-4), 539–558.

Sund, N., Porta, G., Bolster, D., & Parashar, R. (2017). A lagrangian transport eulerian reaction spatial (laters) markov model for prediction of effective bimolecular reactive transport. Water Resources Research, 53(11), 9040–9058.

Svensk Kärnbränslehantering AB. (2010). Data report for the safety assessment SR-site (TR-10-52) (Tech. Rep.). Svensk Kärnbränslehantering AB.

Sweeney, M. R., & Hyman, J. D. (2020). Stress effects on flow and transport in three-dimensional fracture networks. J. Geophys. Res. Sol. Ea., in press. doi: 10.1029/2020JB019754

Valera, M., Guo, Z., Kelly, P., Matz, S., Cantu, V. A., Percus, A. G., . . . Viswanathan, H. S. (2018). Machine learning for graph-based representations of three-dimensional discrete fracture networks. Computational Geosciences, 22(3), 695–710.

Valocchi, A. J., Bolster, D., & Werth, C. J. (2019). Mixing-limited reactions in porous media. Transport in Porous Media, 130(1), 157–182.

Viswanathan, H. S., Hyman, J., Karra, S., O'Malley, D., Srinivasan, S., Hagberg, A., & Srinivasan, G. (2018). Advancing graph-based algorithms for predicting flow and transport in fractured rock. Water Resources Research, 54(9), 6085–6099.

Werth, C. J., Cirpka, O. A., & Grathwohl, P. (2006). Enhanced mixing and reaction through flow focusing in heterogeneous porous media. Water Resources Research, 42(12).

Wood, B. D., Quintard, M., & Whitaker, S. (2000). Jump conditions at non-uniform boundaries: the catalytic surface. Chemical Engineering Science, 55(22), 5231–5245.

Wright, E. E., Richter, D. H., & Bolster, D. (2017). Effects of incomplete mixing on reactive transport in flows through heterogeneous porous media. Phys. Rev. Fluids, 2(11), 114501.

Zimmerman, R. W., & Bodvarsson, G. S. (1996). Hydraulic conductivity of rock fractures. Transport Porous Med., 23(1), 1–30.